JOURNAL OF THE AMERICAN CHEMICAL SOCIETY

Journal of the American Chemical Society is published by the American Chemical Society. 1155 Sixteenth Street N.W., Washington, DC 20036

J|A|C|S
ARTICLES

Structural Features of the Modulated $BiCu_2(P_{1-x}V_x)O_6$ Solid Solution; 4-D Treatment of $x = 0.87$ Compound and Magnetic Spin-Gap to Gapless Transition in New Cu^{2+} Two-Leg Ladder Systems

Olivier Mentré,*,† El Mostafa Ketatni,‡ Marie Colmont,† Marielle Huvé,†
Francis Abraham,† and Vaclav Petricek§

*Contribution from the Laboratoire de cristallochimie et physicochimie du solide de Lille,
UMR CNRS No. 8012 - ENSCL, BP 108 - 59650 Villeneuve d'Ascq, France, Laboratoire
d'Electrochimie et chimie des matériaux, Faculté des Sciences et Techniques, BP 523,
Béni Mellal, Morocco, and Institute of Physics, Academy of Sciences of the Czech Republic,
18221 Praha, Czech Republic*

Received May 4, 2006; E-mail: mentre@ensc-lille.fr

Abstract: The $BiCu_2(P_{1-x}V_x)O_6$ system shows the appearance of various phenomena that progressively change as a function of the average $(P/V)O_4$ groups size. Then, from $x = 0$ to $x \approx 0.7$, a solid solution exists with respect to the basic orthorhombic unit cell of $BiCu_2PO_6$. For greater x values ($0.7 < x < 0.96$), structural modulations with incommensurate q vector that slightly change versus x appear. The 4-D treatment of single-crystal XRD data of the modulated phase corresponding to $x = 0.87$ at 100 K (orthorhombic, $a = 12.379(3)$Å, $b = 5.2344(9)$ Å, $c = 7.8270(14)$ Å, $q = 0.268(3)$ b*, super space group: $Xbmm(0\gamma0)$ s00, X stands for the nonprimitive centering vector (1/2,0,1/2,1/2), $R(\text{obs})_{\text{overall}} = 5.27\%$, $R(\text{obs})_{\text{fundamental}} = 4.48\%$, $R(\text{obs})_{\text{satellite}} = 6.58\%$) has evidenced strong positional modulated effects within the $[BiCu_2O_2]^{3+}$ ribbons while three XO_4 configurations compete along the x_4 fourth dimension. There is no P/V segregation along x_4 in good agreement with steric-only origins of the modulation. Finally for $0.96 < x < 1$, two phases coexist, i.e., $BiCu_2VO_6$ ($X = 1$) and a modulated phase of the previous domain.The $BiCu_2VO_6$ crystal structure shows a unit cell tripling associated with monoclinic symmetry lowering. The VO_4 orientations between two ribbons proceed with respect to the interribbon distance. Then the full system shows flexible interactions between modulated Bi/M/O-based ribbons and surrounding tetrahedral groups, depending on the average XO_4 size. Furthermore, between two ribbons the Cu^{2+} arrangement forms magnetically isolated zigzag copper two-leg ladders. Our preliminary results show a spin-gap behavior likely due to the existence of true $S = {}^1/_2$ Heisenberg two-leg ladders. Modulated compositions are gapless, in good agreement with band-broadening toward a continuum in the magnetic excitation spectrum. The continuous distribution of Cu−Cu distances along the rungs and legs of the ladders should be mainly responsible for this magnetic change.

Introduction

The investigation of double Bi^{3+}/M^{2+} oxide vanadophosphate compounds led to a number of new materials that show original crystal structures.[1−9] Among these series, a large part show well-ordered frameworks with various Bi^{3+}/M^{2+} arrangements driving their electric/magnetic properties. Indeed, the $M = Cu^{2+}$ case has been essentially studied, providing interesting examples of magnetic low-dimensional systems. Then $Bi_4Cu_3V_2O_{14}$ exhibits magnetic interactions in a way that can be regarded as a three-leg ladder with diagonal interactions system.[10−11] Differently, $BiCu_2VO_6$ which exhibits zigzag two-leg copper ladders shows a complex narrow-band spin-gap behavior that may be due to due to the existence of three different dimer types along the ladder axis, or $S = {}^1/_2$ spin-ladders.[12,13] Within the

---

[†] Laboratoire de cristallochimie et physicochimie du solide de Lille.

[‡] Laboratoire d'Electrochimie et chimie des matériaux, Faculté des Sciences et Techniques.

[§] Institute of Physics, Academy of Sciences of the Czech Republic.

(1) Mizrahi, A.; Wignacourt, J. P.; Steinfink, H. *J. Solid State Chem.* **1997**, *133*, 516.

(2) Mizrahi, A.; Wignacourt, J. P.; Drache, M.; Conflant, P. *J. Mater. Chem.* **1995**, *5*, 901.

(3) Tancret, N. PhD Dissertation, Université des Sciences et Technologies de Lille, France, September 1995.

(4) Radosavlejevic, I.; Evans, J. S. O.; Sleight, A. W. *J. Solid State Chem.* **1998**, *141*, 149

(5) Xun, X.; Uma, S.; Yokochi, A.; Sleight, A. W. *J. Solid State Chem.* **2002**, *167*, 245.

(6) Radosavlejevic, I.; Howard, J. A. K.; Evans, J. S. O. *J. Mater. Chem.* **2002**, *12*, 2648.

(7) Radosavlejevic, I.; Howard, J. A. K.; Whithers, R. L.; Evans, J. S. O. *Chem. Commun.* **2001**, *19*, 1984.

(8) Giraud, S.; Mizrahi, A.; Drache, M.; Conflant, P.; Wignacourt, J. P.; Steinfink, H. *Solid State Sci.* **2001**, *3*, 593.

(9) Labidi, O.; Wignacourt, J. P.; Roussel, P.; Drache, M.; Conflant, P.; Steinfink, H. *Solid State Sci.* **2004**, *6*, 783.

(10) Sakourai, H.; Yoshimura, K.; Kosuge, K.; Tsujii, N.; Abe, H.; Kitazawa, H.; Kido, G.; Michor, H.; Hilsher, G. *J. Phys. Soc. Jpn.* **2002**, *71*, 1161.

(11) Okubo, S.; Hirano, T.; Inagaki, Y.; Ohta, H.; Sakurai, H.; Yoshimura, H.; Kosuge, K. *Phys. Rev. B: Condens. Mater. Phys.* **2004**, *346−347*, 65−69.

10.1021/ja0631091 CCC: $33.50 © 2006 American Chemical Society

common description, its crystal structure is formed by the association of MO_x and VO_4 tetrahedra, the Bi^{3+} cations being considered as interstitial. Therefore, the recent discovery of non-stoichiometric disordered compounds in the Bi_2O_3-MO-P_2O_5 systems, e.g. Bi−1.2M−1.2$PO_{5.5}$ (M = Co, Zn, Mn),[14] Bi−6.2Cu−6.2P_5O_{28},[15] Bi−3Cd−3.72M−1.128P_3O_{17} (M = Co, Cu, Zn)[16]..., etc., has shown strong topological relationships between all of the isolated compounds (ordered or not) which can be described by the association of $(Bi,M)_4O$ tetrahedra into infinite ribbons of various widths. The occupancy of edges of ribbons by M^{2+} only or mixed Bi^{3+}/M^{2+} cations yields either ordered materials or strongly disordered compounds, generally differentiated by a competition (disordered case) or not (ordered case) between several surrounding PO_4 configurations around the central P positions.[14] At this stage, it is necessary to recall that to cast off refinement problems due to the disorder, we developed a high-resolution electronic microscopy (HREM) code able to establish the sequence of ribbons and to view the main crystal structure prior to XRD refinement.[17] For these materials, the observation of (commensurate or not) satellite spots in electron diffraction (ED) and/or X-ray diffraction (XRD) patterns has been intuitively associated to a fully Bi^{3+} versus M^{2+} ordering at the edges of ribbons and to subsequent PO_4 periodic ordering. In this paper, we demonstrate that the situation may not be so clear and that partial ordering can dominate. Toward this aim, we investigated the so-called "ordered compound" system of formulas $BiCu_2(P_{1-x}V_x)O_6$. By analogy to the prior ribbon-based description, the BiM_2XO_6 crystal structure can be regarded as the arrangement of double ribbons (two-tetrahedra wide) surrounded by XO_4 groups. Bi^{3+} occupy the centers of ribbons, and Cu^{2+}, the edges of ribbons. It is noteworthy that $BiCu_2VO_6$ crystallizes in a triple monoclinic supercell by comparison with the orthorhombic unit cell for $BiCu_2PO_6$[12].[18] In intermediate domains ($0.7 < x < 0.96$), satellite spot positions are modified, yielding the modulation vector $q \approx 0.27$ b*. It strongly suggests XO_4 ordering and possible V/P segregation. This work reports the examination of q versus x and the structure analysis of modulated regions or the strategic compositions. We especially focused on the description and analysis of the modulated region and on its structural origin by comparison with the end members of the solid solution. A brief analysis of the magnetic susceptibility versus x is also presented by analogy to the structural conclusions. Then, the influence of commensurate ($x = 1$) or incommensurate ($0.7 < x < 0.96$) superstructures on the spin-gap behavior observed in the basic crystal structure ($0 < x < 0.7$) through modification of Cu−Cu separations within the copper ladders appears of particular interest.

Experimental Section

Synthesis. The powder sample corresponding to $BiCu_2P_{1-x}V_xO_6$ ($0 \le x \le 1$) series was synthesized by solid-state reaction between Bi_2O_3, CuO, V_2O_5, and $(NH_4)_2HPO_4$. The mixture was heated at 160, 300, 500 °C, and finally at 780 °C for 2 days in an alumina crucible in air. Several intermediate regrindings were necessary to obtain pure materials. Crystals of various compositions have been prepared by melting and controlled cooling (3 °C/h) of powders. Note the stoichiometric change during crystallization, e.g: single crystals of $x = 0.87$ and $x = 0.32$ obtained from powders from $x = 0.8$ and 0.6 respectively due to uncongruent melting.

Single-Crystal Data Collection. XRD data collection has been performed on a Bruker SMART 100 K diffractometer (Mo Kα = 0.7107 Å). A full sphere of the reciprocal space has been collected using 600 × 0.3° wide ω-scan frames (at $\varphi = 0°, 120°$, and 240 °) with a sample−detector separation of 5.4 cm. For $x = 0.87$, the crystal was cooled to 100 K using a OXFORD SYSTEMS 700 cryostem cooler to limit the atomic thermal motion. The incommensurate modulation vector refinement yields $q = 0.273(1)$ b* at room temperature and 0.268(3) b* at 100 K using Nada.[19] Intensities have been extracted using SAINT 7.0.[20] After all pertinent corrections, four indices (*hklm*) data have been corrected for absorption using the crystal face indexation and the Gaussian method option implanted in Jana 2000.[21]

Electron Microscopy. Electron diffraction patterns (EDP) were obtained on a JEOL 200CX. In any case, the materials have been crushed and dispersed on a holey carbon film deposited on a Cu grid.

Other Techniques. Powder XRD was performed on a Siemens D5000 diffractometer. The neutron diffraction data have been collected at the Institut Laüe Langevin (ILL), Grenoble, France, on the D1a diffractometer, $\lambda = 1.909$ Å. The magnetic susceptibilities have been measured using a superconducting quantum interference device (SQUID) Quantum Design magnetometer, on cooling under an applied field of 0.5 T. To determine the g values of the $S = {}^1/_2$ Cu^{2+} ions, EPR spectra were collected with a Bruker ELEXYS 580 spectrometer operating at 100 kHz.

Structural Generalities

The $BiCu_2P_{1-x}V_xO_6$ compounds are mainly isostructural with other BiM_2XO_6 compounds (M = Mg, Ca, Zn, Cu, Pb, ..., etc.), (X = P, V, As) reported so far.[1−9] Within these series of compounds, a doubt subsists about the true space group. As discussed in the reference,[22] the XO_4 motion able to bring tetrahedra out of some symmetry elements may generate a symmetry lowering in respect to the symmetrical Bi-M−O based framework. In the $a \approx 11.5$ Å, $b \approx 5.2$ Å, $c \approx 7.8$ Å cell orientation, the reported space groups at room temperature are generally either *Pnma* or *Bbmm* distinguished by a slight XO_4 reorientation. In the $BiMg_2VO_6$ case,[23] the centering displacive transition from one form to the other one at 350 K, clearly shows the difficulty to establish true space groups from powder X-ray diffraction (XRD) patterns only, while neutron diffraction (ND) is more relevant. For instance, the ND reexamination of $BiMg_2PO_6$[24] yields the *Pnma* space group instead of the previously announced *Bbmm* from powder XRD analysis.[25] As a matter of fact, in *Pnma* four independent oxygen atoms (multiplicity: 1+1+1+1) constitute the XO_4 tetrahedron versus three independent oxygen atoms (multiplicity: 2+1+1) in *Bbmm*, and

---

(12) Radosavljevic, I.; Evans, J. S. O.; Sleight, A. W. *J. Solid State Chem.* **1998**, *141*, 149.
(13) Masuda, T.; Zheludev, A.; Kageyama, H.; Vasilev, A. N. *Europhys. Lett.* **2003**, *63*, 757.
(14) Abraham, F.; Cousin, O.; Mentre, O.; El Ketatni, M. *J. Solid State Chem.* **2002**, *167*, 168.
(15) El Ketatni, M.; Huve, M.; Abraham, F.; Mentre, O. *J. Solid State Chem.* **2003**, *172*, 327.
(16) Colmont, M.; Huve, M.; El Ketatni, M.; Abraham, F.; Mentre, O. *J. Solid State Chem.* **2003**, *176*, 221.
(17) Huve, M.; Colmont, M.; Mentre, O. *Chem. Mater.* **2004**, *16*, 2628.
(18) Abraham, F.; Ketatni, M.; Mairesse, G.; Mernari, B. *Eur. J. Solid State Chem.* **1994**, *31*, 313.
(19) Schönleber, A.; Meyer, M.; Chapuis, G. NADA: A computer program for the simultaneous refinement of orientation matrix and modulation vector-(s). *J. Applied Crystallogr.* **2001**, *34*, 777.
(20) *Saint 7*; Bruker Analytical X-ray Systems: Madison, WI, 2000.
(21) Petricek, V.; Dusek, M.; Palatinus, L. *Jana 2000*; Institute of Physics: Praha, Czech Repubic, 1997.
(22) El Ketatni, M.; Mernari, B.; Abraham, F.; Mentre, O. *J. Solid State Chem.* **2000**, *153*, 48.
(23) Radosavljevic, I.; Sleight, A. W. *J. Solid State Chem.* **2000**, *149*, 143.
(24) Radosavljevic, I.; Howard, J. A. K.; Sleight, A. W. *Int. J. Inorg. Mater.* **2000**, *2*, 543.
(25) Huang, J.; Gu, Q.; Sleight, A. W. *J. Solid State Chem.* **1993**, *105*, 599.

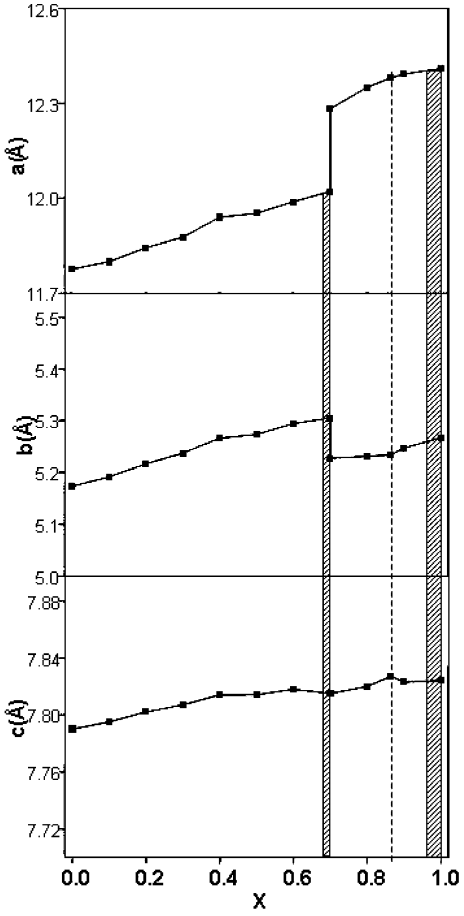

Figure 1. Variation of the lattice parameters for $BiCu_2P_{1-x}V_xO_6$ versus *x*. The vertical line shows the investigated crystal composition.

within a slight approximation both symmetries lead to the real XO_4 orientation.

Subdivision in Three Domains. The lattice parameters versus *x* for $BiCu_2(P_{1-x}V_x)O_6$ are shown on the Figure 1. In this figure, the basic metric orthorhombic unit cell parameters are considered even for $x = 1$, for which a monoclinic symmetry is effective. The $x = 0.7$ composition shows a mixture of two border phases mainly distinguishable by the **a** and **b** parameters. At both sides of this "transition" limit, **a**, **b**, and **c** progressively increase versus *x*. The observed transition is then characterized by an abrupt *a*-axis dilatation and *b*-axis contraction. In the vanadium-rich part of the diagram, fine examination of the $x = 0.96$ XRD pattern shows the existence of two phases assigned to $x = 0.95$ and $x = 1$. Then, along the V for P substitution, three subsequent domains can be identified.

$0 \leq x < 0.7$. The compounds adopt the $BiCu_2PO_6$ ($x = 0$) crystal structure. This latter has been refined in the *Pnma* space group from XRD single-crystal data.[18] ND data and ED patterns confirm the conservation of the primitive lattice until the $x = 0.7$ border limit. The [101] zone axis ED pattern for $x = 0$ is shown in Figure 2a. The shift and difference of periodicity between the zero and first-order Laue zone (ZOLZ and FOLZ) patterns confirm the *Pnma* space group valid for the full $0 \leq x < 0.7$ compositional range. The crystal structures have been refined for $x = 0.32$ from single-crystal XRD data ($R_F = 2.66\%$, $wR_F = 2.51\%$) and for $x = 0.6$ from powder ND data (wBragg *R* factor = 4.89%, wR_F factor = 3.20%). For the former, data collection and refinement parameters are reported in Table 1.

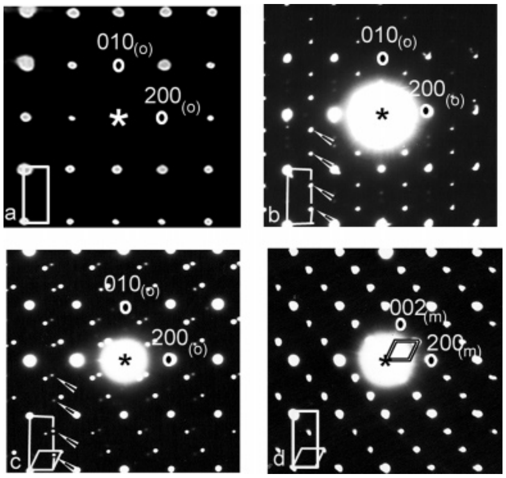

Figure 2. [101] ED patterns for several compositions: (a) $x = 0$ basic orthorhombic cell. No extra phenomenon is evidenced. (b) $x = 0.7$. The indexation is given in the previously basic orthorhombic cell (o). White arrows indicate satellite spots compatible with a modulation vector $q = 1/4$ b*. (c) $x = 0.8$ The indexation is given in the previously basic orthorhombic cell (o). $q \approx 0.3$ b*. (d) $x = 1$. The monoclinic cell related to the orthorhombic one is evidenced. The indexation is given in the monoclinic cell (m).

The atomic coordinates and the Rietveld refinement data are given in the Supporting Information. The pertinent bond lengths are gathered in Table 2 for $x = 0$, 0.32, and 0.6. The crystal structure shows no drastic changes. We can only observe the (P/V)−O bonds increase versus *x*, e.g. average X−O = 1.54 Å for $x = 0$ and 1.63 Å for $x = 6$. However, the XO_4 mean orientation with regard to the Bi/Cu/O framework remains unchanged. The copper two-leg ladders especially discussed in the magnetic section remain nearly unchanged. Thus, in this domain the V substitution for P is possible without any structural modification despite the increase in XO_4 size, which is compensated by the lattice dilatation.

$0.7 < x \leq 0.95$. This domain is characterized by drastic *a*- and *b*-axes jumps. In this domain the B centering is well respected as confirmed by the absence of *hkl*, $h+l = 2n+1$ reflections still observable for $x = 0.6$ on ED patterns and ND powder data. However an additional set of satellite spots is clearly observed. Parts b and c of Figure 2 exhibit the satellite spots for $x = 0.7$ (one of the two coexisting phases) and 0.8, respectively. For the former, the exact superposition of the second-order satellites yields the commensurate modulation vector $\mathbf{q} = 1/4$ b*, under the ED resolution approximation. For the latter **q** deviates to the incommensurate ∼0.3 b* value as evidenced by second-order satellite pairs. The satellite peaks are barely observable on XRD powder patterns but are evidenced on ND patterns by weak lines. For $x = 0.8$ and 0.9, **q** was refined to 0.279(3) b* and 0.294(3) using the profile fitting mode implanted in Jana 2000.[21] Prior to these refinements, it has been checked on ED patterns that the satellite existence conditions are compatible with the super space group *Xbmm*($0\gamma0$) s00 used for the 4D treatment of the $x = 0.87$ case, see next section.

$0 < x < 0.96$. As already reported, in this narrow domain the fine examination of XRD patterns indicates no P/V solid solution since two compounds coexist. Figure 3 shows the splitting of diffraction lines for $x = 0.96$ that correspond to the mixture of one modulated phase of the previous domain ($x \approx 0.95$) and $BiCu_2VO_6$. For this composition, the crystal structure has first been refined from single-crystal data analysis in a

Table 1. Data Collection and Refinement Parameters for $x = 0.32$ and 0.87 Using Both the 3D and the 4D Approach for the Latter

	$BiCu_2(V_{0.32}P_{0.68})O_6$	$BiCu_2(V_{0.87}P_{0.13})O_6$	
Crystal Data			
crystal symmetry	orthorhombic	orthorhombic	
space group, super space group	*Pnma*	*Bbmm*, $Xbmm(0\gamma0)$ s00	
unit cell (Å)	$a = 11.884(3)$ $b = 5.237(1)$ $c = 7.809(2)$	$a = 12.379$ (2) $b = 5.2344(9)$ $c = 7.8270(14)$	
modulation vector	none	$q = 0.268(3)$ b*	
Z	4	4	
MW (g/mol), μ (mm^{-1}) for Mo Kα	469.46, 44.14	480.44, 43.13	
Data Collection			
diffractometer	Bruker CCD 1 K	Bruker CCD 1 K	
radiation Mo Kα (Å)	0.71073	0.71073	
scan mode	ω-scans	ω-scans	
recorded angular range θ (deg)	3.12−28.93	3.08−29.37	
recording reciprocal space	$-15 \leq h \leq 15$ $-7 \leq k \leq 7$ $-10 \leq l \leq 10$	$-16 \leq h \leq 16$ $-6 \leq k \leq 7$ $-10 \leq l \leq 10$ $-1 \leq m \leq 1$	
number of ind. measured reflections		3D approach	4D approach
	589	388	1093 main: 388 satellites: 705
crystal morphology (distance in mm to the crystal center)	0 1 0, 0 $\bar{1}$ 0: 0.240 1 0 1, $\bar{1}$ 0 $\bar{1}$: 0.012 $\bar{1}$ 0 1, 1 0 $\bar{1}$: 0.018	1 0 0, $\bar{1}$ 0 0:0.014 0 1 0, 0 $\bar{1}$ 0:0.210 0 0 1, 0 0 $\bar{1}$:0.015	
transmission factor range (T_{min}/T_{max} (%))	4/38	2/33	
R merging factor (%)	3.64	main: 8.72; satellites: 11.09	
Refinement Parameters	3D		4D
	least squares on F, JANA 2000		
number of refined parameters	52	49	54
weighting scheme	$1/\sigma^2$		$1/\sigma^2$
R, wR [$I > 3\sigma(I)$] (%)	2.66, 2.51	4.88, 5.81	overall: 5.26, 6.00 main: 4.45, 5.45 satellites: 6.60, 6.93
max/min $\Delta\rho$ e/Å^3	2.10/−2.37	3.8/−3.4	5.1/−5.9

Table 2. Pertinent Interatomic Distances in the *Pnma* Domain ($0 \leqslant x < 7$)[a]

	$x = 0$[b]	$x = 0.32$	$x = 0.6$
	Bi−O Polyhedron		
Bi−O1 (2 x)	2.189(6)	1.989(5)	2.193(4)
−O1 (2 x)	2.361(6)	2.358(6)	2.338(4)
−O4	2.487(9)	2.527(9)	2.574(4)
	Cu1 Square Pyramid		
Cu1−O1 (2 x)	1.937(6)	1.956(6)	1.960(4)
−O2 (2 x)	2.024(7)	2.015(5)	2.000(4)
−O4	2.189(9)	2.174(9)	2.190(4)
	Cu2 Square Pyramid		
Cu2−O1 (2 x)	1.936(6)	1.947(6)	1.952(4)
−O2 (2 x)	2.003(7)	1.989(5)	1.982(4)
−O3	2.35(1)	2.34(1)	2.345(4)
	Ladders		
Cu1−Cu2 ⊥	2.896(2)	2.881(2)	2.873(4)
Cu1−Cu2//	3.214(1)	3.220(1)	3.220(2)
XO $_4$ tetrahedra			
(P/V)−O2 (2 x)	1.564(7)	1.613(6)	1.702(7)
−O3	1.52(1)	1.561(9)	1.60(1)
−O4	1.526(9)	1.589(8)	1.51(1)

[a] The ⊥ and || symbols for Cu−Cu separations refer to the copper ladders growing axis (= *b*). [b] Taken from ref 18.

distorted monoclinic triple cell with the geometric relations $\vec{a}_{mono} = \vec{a}_{ortho} - \vec{b}_{ortho}$; $\vec{b}_{mono} = -\vec{c}_{ortho}$; $\vec{c}_{mono} = 3\vec{b}_{ortho}$, $a = 13.4932(1)$ Å, $b = 7.8224(1)$ Å, $c = 15.7972(1)$ Å, $\beta = 113.113(1)°$, space group $P2_1/n$.[12] Over several crystallographic modifications, the distortion mainly induces the splitting of the two independent Cu_{1-2} (for $x = 0$) into six independent Cu_{1-6} copper atoms ordered along copper zigzag ladders that will be extensively discussed below. In our work, the reported crystal structure for $BiCu_2VO_6$ has been successfully refined from powder neutron diffraction data using Fullprof 2000,[26] wBragg R factor = 4.35%, wR_f factor = 2.57%. Note that a recent study has shown a displacive $P2_1/n$ to $I2/m$ transition at 500 K for this compound, once more driven by PO_4 librational motions.[27] The $x = 1$ [101] zone axis ED pattern of the Figure 2d shows characteristic features of the unit cell tripling associated with the orthorhombic to monoclinic symmetry lowering for $BiCu_2VO_6$. Then the extra spots between d and a of Figure 2 only picture this distortion while the full pattern (ZOLZ+FOLZ) respects the $P2_1/n$ extinctions. Table 3 reports the refined lattice parameters, modulation vectors, and symmetries for the $BiCu_2(P_{1-x}V_x)O_6$ system.

The $x = 0.87$ 4-D Single-Crystal Analysis. Average Crystal Structure. The average crystal structure has been refined in the *Bbmm* space group from the data collected at 100 K. The final R values are $R_1(obs) = 4.88\%$, $wR_1(obs) = 5.81\%$. Data collection and refinement data for both the average and

---

(26) Rodriguez-Carjaval, J. *Fullprof 2000*; LLB (CEA-CNRS): France 2000.
(27) Radosavljevic, I.; Evans, J. S. O.; Tao, S.; Irvine, T. S. *J. Solid State Chem.* **2005**, *178*, 2825.

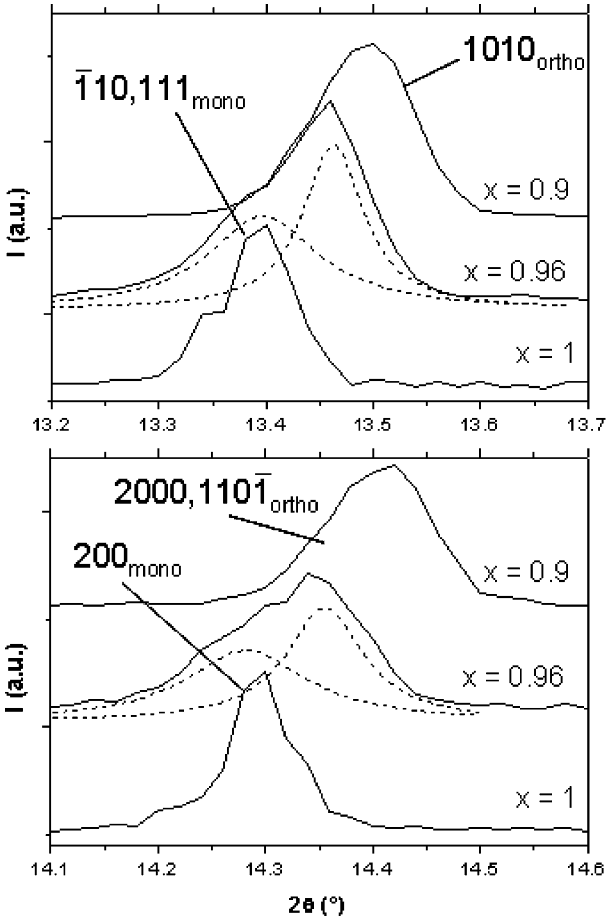

Figure 3. Evidence of two phases for the $x = 0.96$ composition. It is formed of $x = 1$ (monoclinic triple unit cell) and $x = 0.95$ compounds (orthorhombic modulated cell).

modulated structure are listed in Table 1. The atomic coordinates are listed in Table 4. The following results characterize the refinement:

(1) Several independent tetrahedral O_4 configurations are observed surrounding the central mixed P/V site. At least three of them are clearly visible with various ratios, Figure 4a−c. Therefore, residual electronic density maxima at correct distances from the central P/V position indicate a stronger disorder. In a first approximation, we can distinguish three PO_4 configurations: tetra-1 with an occupancy of 0.5 and tetra-2/tetra-2m with an occupancy 0.25/0.25 where m stands for a symmetrical relation ship through a mirror plane perpendicular to *b*.

(2) The P/V refined ratio is 0.13/0.87 in good agreement with the *x* value deduced from the unit cell parameters, Figure 1. At this stage, the main interrogations which justify our 4D treatment deal with the possible or not possible P/V ordering and with the XO_4 configurational ordering or not in the incommensurate supercell along *b*.

4-D Approach. Considering the refined $q = 0.268$ b* and the observed systematic extinctions: *hklm*: $h+l+m = 2n$ and *0klm*: $k + m = 2n$, the only compatible super space group is $Xbmm(0\gamma0)$ s00 where *X* denotes the superspace centering $1/2x + 1/2z + 1/2x_4$. In a first stage, first-order displacement modulation waves are applied to Bi, P/V, Cu, and O1 (ribbons) while a modulation of anisotropic temperature parameters is applied to Bi only. The refinement yields *R*(obs) overall = 6.46%, $R(\text{obs})_{\text{fundamental}} = 4.96\%$, $R(\text{obs})_{\text{satellite}} = 8.96\%$. This indicates the major role of the heavy atoms displacive modulation and questions about the possible P/V ordering. Then occupancy modulation is applied to P and V under a restriction of full occupancy along the x_4 coordinate. As shown on the Figure 5a, the flat shape of V and P occupancies versus *t* indicates a complete P/V disorder in the superspace (where $t = x_4 - \vec{q}\cdot\vec{r}$: q^* is the modulation vector and *r* an average position in physical space). For a good understanding, keep in mind that an increment of 0.268 along *t* in the 4D-space corresponds to a translation from one cell to the next one along *b* in the real space. At this stage the P/V occupancies are about 0.17/0.83.

XO_4 Segregation in Three x_4 Domains. The introduction of occupancy modulations for XO_4 corners, namely O2, O3, O3′, and O4 without any restriction yields results shown on the Figure 5b. Then, the most remarkable behavior concerns O3 and O3′ that show complementary occupancies versus *t*. The O3 maximal occupancy is assorted with O2 and O4 half occupancies. This plots pictures well a separation along x_{40} of two subsequent domains, as already postulated from the average crystal structure. Figure 6 shows the (*y*,*x*4) Fourier difference sections for O3 and O3′ before oxygen introduction, also in agreement with the O3′/O3 occupational complementarity along the fourth dimension.

(i) The first domain *t* is centered around $x_{40} = 1/4$ and adopts a unique configuration of $P/V(O3'_2O2_2)$ (= tetra-1). The x_{40} value can be deduced from Figure 5 using the relation $t = x_4 - q\langle r\rangle$, e.g. for O3′, $t_{max} \approx 0.18$, $q = 0.268$ b*, and $y = 1/4$.

(ii) The second domain is centered around $x_{40} = 3/4$ ($t \approx 0.68$). In this domain (referring to the average structure) would coexist two $P/V(O2O3O4_2)$ tetrahedra related by a mirror plane perpendicular to *b*, i.e., = tetra-2 and tetra-2_m. Of course, this model is ideal, and several interrogations remain. However, a more careful observation of the tetrahedral environment gives good clues of an additional separation within this region. In fact, in the 4D space, according to the super space group symmetry, the mirror plane perpendicular to *b* is associated with transformation along x_4 as follows: $x, y, z, x_4 \rightarrow x, 1/2 - y, z, 1/2 - x_4$. It involves a tetra-2/ tetra-2 $_m$ separation in different unit cells along x_4. It is also observable from the shift between O2/O4 and $O2_m/O4_m$ in two parts where tetra-2_m and tetra-2 predominate respectively, Figure 5b. Of course this separation is unavailable for tetra-1 since it is invariant by the *m* perpendicular to *b* symmetry.

Molecular Model for XO_4. In Figure 6 one should also note the large *y* displacement amplitude along x_4 for O3′. This kind of phenomenon (also true for *x* and *z*) associated with imprecision due to the weak weight of partially occupied oxygen positions artificially creates significant distortion of tetrahedra at particular x_4 sections. Despite the good quality of the refinement using the atomic model, $R(\text{obs})_{\text{overall}} = 5.09\%$, $R(\text{obs})_{\text{fundamental}} = 4.55\%$, $R(\text{obs})_{\text{satellite}} = 5.99\%$, it was decided to use regular tetrahedral P/VO_4 molecules through the rigid body option. Then, tetrahedral rigid bodies centered around $x_4 = 0.25$ and 0.75 for tetra-1 and tetra-2, respectively, with the same occupational width. The labeling of XO_4 corners has been performed through the following labeling with respect to perfect

Table 3. Lattice (Super Lattice) Characteristics for $BiCu_2P_{1-x}V_xO_6$

x	a (Å)	b (Å)	c (Å)	q/b*	(super) space group
$0 < x < 0.6^a$	11.776(1)−11.988(2)	5.173(1)−5.294(1)	7.790(1)−7.818(2)	none	$Pnma$
$0.7^{a,b}$	12.021(5) 12.283(4)	5.305(2) 5.227(2)	7.815(2) 7.833(3)	none ∼ 0.25	− $Xbmm$(0b0) s00
0.8^c	12.3127(3)	5.2217(1)	7.8008(1)	0.279(1)	−
0.87^d (rt) (100 K)	12.38(1) 12.379(2)	5.229(9) 5.2234(9)	7.82(1) 7.827(1)	0.272(5) 0.268(3)	− −
0.9^c	12.3759(5)	5.2370(2)	7.8147(3)	0.295(1)	−
$0.96^{a,b}$ + $BiCu_2VO_6$	12.3923(5)	5.2601(2)	7.8216(3)	∼ 0.30	−
1^a	13.4932(2) ($\vec{a}_{ortho}-\vec{b}_{ortho}$)	7.8224(1) ($\vec{c}_{ortho}$) $\beta = 113.113(1)°$	15.7972(1) ($3\vec{b}_{ortho}$)	none	$P2_1/n$

[a] From powder XRD data least-squares refinement. [b] q cannot be accurately refined from XRD powder data within a multiphased sample. $q = 0.25$ b* is estimated from ND patterns. [c] From ND powder data profile fitting using Jana 2000. [d] From single-crystal XRD using Nada.

Table 4. Refined Values of Coordinates and Fourier Amplitudes of the Displacive Modulation Functions for $BiCuP_{0.13}V_{0.87}O_6$ Using Both the 3D and the 4D Treatments[a]

atom	occ./wave	x	y	z	U_{eq}/U_{iso} (Å^2)
		3D Average Structure			
Bi	4c, 1	0.39849(7)	0.75	0	0.026(1)
Cu	8g, 1	0.5765(2)	0.75	0.3089(3)	0.022(1)
2	4c, 0.87(3)/0.13(3)	0.6914(4)	0.25	0.5	0.029(1)
O1	8e,1	0.5	0	0.170(2)	0.026(3)
O2	8f, 0.75	0.385(2)	−0.030(7)	0	0.052(8)
O3	4c, 0.5	0.176(2)	0.25	0	0.029(7)
O3′	8g, 0.5	0.242(3)	0.25	0.180(6)	0.070(14)
O4	16h, 0.25	0.344(3)	0.060(7)	0.169(5)	0.034(8)
		4D Modulated Structure			
Bi	1	0.39792(6)	0.75	0	0.0181(2)
	s,1	0.01584(8)	0	0	
	c,1	0	0.02068(16)	0	
Cu	1	0.57645(13)	0.75	0.3084(2)	0.0199(4)
	s,1	0.00556(18)	0	0.0111(3)	
	c,1	0	−0.0155(3)	0	
O1	1	0.5	0	0.1691(9)	0.017(2)
	s,1	0.0175(9)	0.0010(16)	0	
	c,1	0	0	0.0028(14)	
		Atoms within Tetra-1			
V1/P1	0.87/0.13	0	0	0	0.0200(14)
O11	1	0.1121	0	0.1254	0.062(6)
O12	1	−0.1121	0	0.1254	0.062(6)
O13	1	0	0.2652	−0.1254	0.035(4)
O14	1	0	−0.2652	−0.1254	0.035(4)
		Atoms within Tetra-2			
V2/P2	0.87/0.13	−0.0038	0	0	0.0200(14)
O21	1	−0.0038	0	0.2172	0.039(9)
O22	1	0.1295	0	−0.0724	0.012(6)
O23	1	−0.0647	0.2652	−0.0724	0.029(5)
O24	1	−0.0647	−0.2652	−0.0724	0.029(5)

[a] The waves are sorted by the term (s for sinus, c for cosinus) and harmonic order. Note that the molecular translational and rotational parameters (see Table 4) are applied on tetra-1 and −2 coordinates for real location in the unit cell.

tetrahedral (X−O = 1.7 Å which is the mean distance deduced from the average structure).

$$\text{Tetra-1: } (O3', O3'_{x,y,1-z}, O2, O2_m) \rightarrow (O11, O12, O13, O14)$$

$$\text{Tetra-2: } (O3, O2, O4, O4_{x,y,1-z}) \rightarrow (O21, O22, O23, 24)$$

The thermal parameters have been restrained equally for equivalent oxygen atoms in the average structure. For each molecule, occupancy, rotation, and translation modulation wave have been applied. Then within the rectilinear approximation of rotational displacements, the ideal tetrahedral edifices remain undistorted for small rotational amplitude only, which is likely in our case, considering the good results of the atomic strings

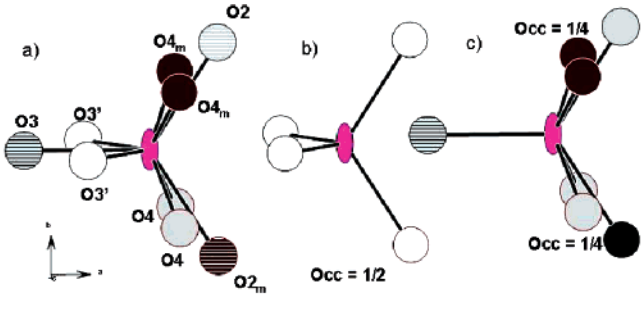

Figure 4. (a) Labeling of the oxygen atoms surrounding the mixed P/V site within the average structure for $x = 0.87$. Evidence of (b) the tetra-1 configuration (white atoms), occupancy = 1/2; (c) the tetra-2 (gray) and tetra-2_m (black).

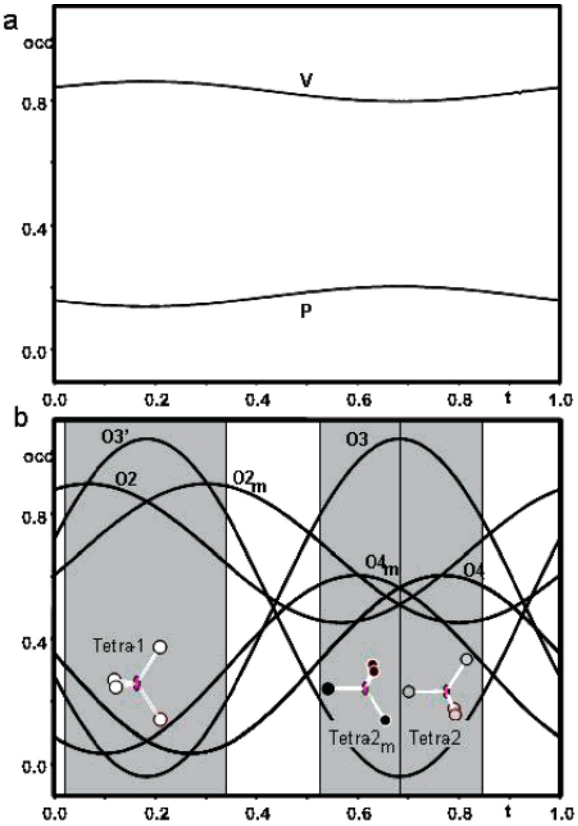

Figure 5. (a) Occupancy modulation for P and V along the fourth dimension *t*. The rather flat lines picture the conservation of a disordered nature for the P/V crystallographic site from one cell to the next one. (b) Occupancy vs *t* for the XO_4 corners assigned to the separation of tetra-1, tetra-2 and tetra-2_m configurations.

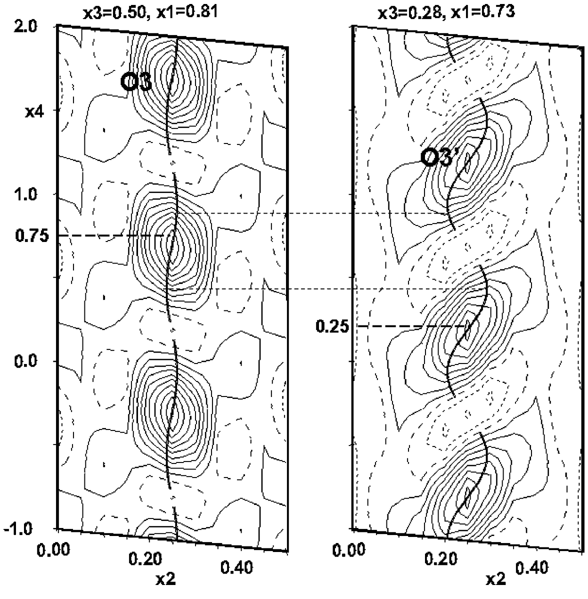

Figure 6. (y,x_4) Fourier difference maps before O3 and O3′ introduction at the $x = 0.81$, $z = 0.5$ and $x = 0.73$, $z = 0.28$ sections showing O3 and O3′ respectively. The superimposed discontinuous lines represent their refined occupancies versus x_4 as shown in Figure 5b.

approach. The relatively large *U* values refined for O11/O12 (= 0.062 Å^2) reflect the *U* value for O3′ in the average structure (= 0.07 Å^2). In that case it is clear that that the modulation string does not perfectly reproduce the XO_4 motion along x_4, due to the low oxygen scattering factors.

Crenel versus Continuous Occupancy. Considering the O3 versus O3′ complementarity versus x_4 (see Figure 6), the validity of Crenel function describing a complete separation between tetra-1, tetra-2, and tetra-2_m along x_4 has been tested. It is noteworthy that the *R* factors are slightly larger as for the final model presented below and that the convergence shows a certain degree of instability. Furthermore, in the refinement the examination of the rotational modulation parameters shows large parameters which strongly distort tetrahedra at the crenel edges. In fact, this effect is probably due to the superposition of the two independent P/VO_4 configurations in this region, in agreement with the necessary use of smooth occupancy functions. Nothing is changed for the central part (around $x_4 = 0.25$ and 0.75) where either tetra-1 or tetra-2/tetra-2_m strongly dominate. As a matter of fact, the chemical origin of the segregation of the two tetrahedral configurations is due to the displacement of the neighboring Bi and Cu. Their displacement modulation being treated with harmonic waves, the use of similar functions for occupancies of P/VO_4 appears justified. Furthermore the use of this Crenel function does not enable the tetra-2/tetra-2_m segregation anymore. Finally, the observation of first-order satellite spots only is comforting the use of continuous functions since the superimposition of Crenel-like occupancies would immediately create satellite reflections of higher order.

The Final Model. The occupancy, rotation, and translation modulations for both molecules are treated using sinusoidal waves. Equations have been used to constrain a full [tetra-1 + tetra-2] occupancy. Within each tetrahedron thermal parameters are restrained equally for corners. At this stage, the centers of both tetra-1 and tetra-2 are located on a 2*mm* site, laying on the mirror plane perpendicular to *b* ($x \approx 0.69$, $y = 1/4$, $z = 1/2$). The refined reliability factors are $R(\mathrm{obs})_{\mathrm{overall}} = 5.58\%$, $R(\mathrm{obs})_{\mathrm{fundamental}} = 4.62\%$, $R(\mathrm{obs})_{\mathrm{satellite}} = 7.18\%$ for 48 refined parameters. It is noteworthy that the simple shift of tetra-2 out of m_y ($x \approx 0.69$, $y \approx 0.245$, $z = 1/2$) improved significantly the fit, $R(\mathrm{obs})_{\mathrm{overall}} = 5.27\%$, $R(\mathrm{obs})_{\mathrm{fundamental}} = 4.48\%$, $R(\mathrm{obs})_{\mathrm{satellite}} = 6.58\%$ for 54 refined parameters. These results are consistent with the tetra-2/tetra-2_m separation in the x_4 space, now accompanied by a true separation of their centroids (P/V)/$(P/V)_m$. Of course, this shift is virtually traduced by an unlikely large tetra-2 to tetra-2_m split in some unit cells, i.e., a competition between two groups far from each other. However the minimal (P/V) − $(P/V)_m$ separation (∼0.024 Å) is obtained at $t = 0.68$, i.e., $x_4 = 0.75$ where the tetra-2/tetra-2_m mixture is maximal, while greater separations are measured in zones where only one tetra-2 configuration should coexist with tetra-1 (see additional explanations in the Supporting Information). Finally, this effect could denote the use of a too symmetrical superspace group; however as already mentioned in the text, the lowering of symmetry is not viewable, considering the collected data. The refined values of coordinates and Fourier amplitudes of the displacive modulation functions are listed in Table 4. Final values of the molecular parameters for tetra-1 and tetra-2 are reported in Table 5. In this table, $\varphi/U_{\mathrm{r}\ x-y-z}$ and $x-y-z/U_{\mathrm{t}\ x-y-z}$ denote the rotational and translational operations applied to a tetrahedral model to bring its corners on the corresponding oxygen atoms of the structure.

Description and Discussion

Structure of the Ribbons. The ideal crystal structure for $BiCu_2XO_6$ compounds is shown in Figure 7a. Here, double

Table 5. Refined Molecular Parameters for Tetra-1 and Tetra-2[a]

	pos. wave	ψ(deg)/U_{rx}	(deg)/U_{ry}	(deg)/U_{rz}	x/U_{tx}	y/U_{ty}	z/U_{tz}	occ. wave	
Tetra-1		180	90	180	0.6872(18)	0.25	0.5	occ.	0.53(2)
	s,1	0	0	0.001(4)	0	0	0	s,1	0.49(2)
	c,1	0	−0.039(3)	0	−0.0036(11)	0	0	c,1	0
Tetra-2		−90	0	−90	0.692(4)	0.236(9)	0.5	occ.	0.233(9)
	s,1	0.005(4)	0	0.002(7)	0	−0.031(3)	0	s,1	−0.24(1)
	c,1	0.014(3)	0	−0.006(6)	0	−0.031(3)	0	c,1	−0.17(1)

[a] The rotational parameters ψ, χ, φ are rotation angles around x, y, and z, respectively. The waves are sorted by the term (s for sinus, c for cosinus) and harmonic order. The occupancy related to the tetra-1 and tetra-2 site symmetries are such that Occ. [tetra-1] + 2 x Occ. [tetra-2] = 100%.

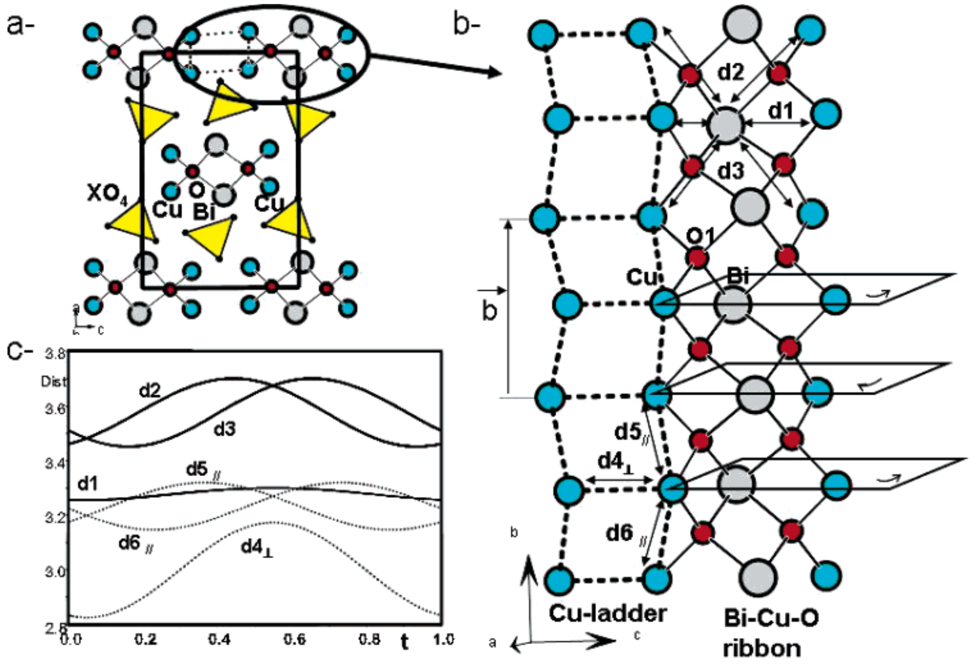

Figure 7. (a) Projection along the b axis of the BiM_2XO_6 crystal structure with evidence of polycationic ribbons surrounded XO_4 groups. The Cu^{2+} zigzag ladders are formed between two ribbons as shown by the dotted lines. (b) Ribbon and ladders growing along the b axis with the distance labeling scheme. (c) Intraribbon and intraladder distances evolution versus the fourth dimension t.

$[BiCu_2O_2]^{3+}$ ribbons, two OBi_2Cu_2 tetrahedra wide, are evidenced surrounded by XO_4^{3-} groups. The zigzag Cu^{2+} two-leg ladders are formed between two ribbons as shown in Figure 7b. The variation of intercationic distances along the fourth dimension is shown in Figure 7c. The analysis of Bi−Cu distances plots (d1, d2, d3) clearly shows that the intraribbon structure is conserved nearly unchanged in the (a,c) plane (see d1 versus t) while strong modification of distances implies atoms at different y levels (see d2 and d3 versus t). As expected, the intraribbon Cu−Cu distances modulation amplitude ($d5_{||}$ and $d6_{||}$ [the || and ⊥ signs indicate the interaction direction in respect to the ladder legs]) follows the d2 and d3 plots. Considering the slight Bi−O1 and Cu−O1 changes along t, see Table 6, it suggests that the structural perturbation within ribbons is performed by the bending of subsequent Bi/Cu layer with regard to the central O(1) layer as schematized on the Figure 7b. The greater motion amplitude is pictured by $d4_{\perp}$ and concerns the interribbons Cu−Cu distances which form rungs of the copper ladder, ranging from 2.824(4) Å to 3.173(4) Å. It clearly shows strong modulations of the inter-ribbon structure in the (a,c) plane. This can be seen as the phenomenon driving the PO_4 ordering along b by the intermediate of their corners that also bonds Cu^{2+} cations.

P/VO$_4$ Partial Ordering. In the $0 \leq x < 0.7$ domain, the average XO_4 size is compatible with a unique XO_4 configuration. In the modulated domain, the continuous occupational modulation functions for XO_4 involves a partial-only ordering of the tetrahedral configurations along t (maximal at $t = 0.18$, 0.61, and 0.76 for tetra-1, tetra-2_m, and tetra-2). The d4 Cu−Cu rung separations are strongly correlated to their closest tetrahedral configurations as presented in the Supporting Information. A fine examination of intermetallic distances as a function of t shows that tetra-1 is associated with the shortest, nearest Cu−Cu bonds, whereas tetra-2 and tetra-2_m are associated with larger surrounding Cu−Cu rungs. Once more, at intermediate t values, mixtures of the two surrounding maxima randomly coexist.

Figure 8 shows the ideal (most probable) orientations of XO_4 groups in subsequent cells along b and their nearest Cu−Cu pairs for $x = 0-0.7$, $0-0.96$ ($q = 0.27$ b*), and 1 (b tripling). As a matter of fact, the unique PO_4 orientation observed in the *Pnma* domain is roughly oriented like tetra-1 ($x = 0.87$) and V_2O_4/V_3O_4 ($x = 1$). It is accompanied with rather short surrounding Cu−Cu distances of 2.89 Å. In the same manner, tetra-1 and V_2O_4/V_3O_4 are systematically involved in short Cu−Cu distances, while on the opposite, tetra-2/tetra-2_m and $V1O_4$ show long neighboring Cu−Cu pairs. Since no P/V segregation occurs along x_4, steric effects only are concerned. The XO_4 corners bond the Cu^{2+} cations. It leads to the alternation of square pyramids and distorted square planes, under the Cu−O

Table 6. Pertinent M−O and Cu−Cu Bond Lengths (Å)

	average	minimal	maximal
M−O: Ribbons			
Bi−O1[a,b,c,d]	2.252(8)	2.248(8)	2.254(7)
Cu−O1[a,c]	1.954(8)	1.946(7)	1.961(9)
O1−O1[b]	2.65(2)	2.60(2)	2.69(2)
O1−O1[k]			
Cu−O (Tetra-1)			
Cu−O11[g]	2.20(3)	2.17(3)	2.23(4)
−O12[h]	2.20(3)	2.17(3)	2.23(4)
−O13[i,j]	1.986(10)	1.933(11)	2.041(14)
−O14[a,k]	1.985(10)	1.933(11)	2.041(14)
Cu−O (Tetra-2)			
Cu−O22[a,k]	1.98(4)	1.93(4)	2.07(5)
−O23[i,l]	2.06(7)	1.96(7)	2.24(6)
−O24[j,m]	2.06(7)	1.96(7)	2.23(6)
M−O: Tetra-1			
V1/P1−O11	1.70(2)	1.70(3)	1.701(19)
−O12	1.70(2)	1.70(3)	1.701(19)
−O13	1.70(3)	1.70(3)	1.70(3)
−O14	1.70(3)	1.70(3)	1.70(3)
M−O: Tetra-2			
V2/P2−O11	1.66(4)	1.63(4)	1.70(4)
−O12	1.66(4)	1.63(4)	1.70(4)
−O13	1.76(7)	1.68(7)	1.84(7)
−O14	1.73(7)	1.66(7)	1.78(7)
Copper Ladder			
$Cu-Cu_{//}$	3.233(2)	3.146(2)	3.319(2
$-Cu_{\perp}$	2.997(3)	2.824(4)	3.173(4)

Symmetry Codes: [a] *x*,1+*y*,1+z. [b] 1−*x*,1−*y*,1−z. [c] 1−*x*,1/2+*y*,1+z. [d] *x*,1/2−*y*,1−*z*. [e] −1/2+*x*,1+*y*,1/2+*z*. [f] −1/2+*x*,1/2−*y*,3/2−*z* [g] 3/2−*x*,1−*y*,3/2−*z*. [h] 3/2−*x*,1/2+*y*,1/2+*z*. [i] *x*,*y*,1+*z* [j] *x*,3/2−*y*,2−*z*. [k] *x*,1/2−*y*,2−*z*. [l] *x*,3/2−*y*,1+*z*. [m] *x*,*y*,2−*z* [n] *x*,*y*,1−*z*. [o] *x*,1/2−*y*,*z*. [p] 1−*x*,−1/2+*y*,*z*. [q] 1−*x*,1/2+*y*,*z*. [r] *x*,3/2−*y*,3−*z*.

< 2.5 Å restriction, due to the XO_4 multi-orientations and slight rotational modulations. Of course, this is possible because of Cu^{2+} variable Jahn−Teller effects.

The lattice parameters change versus *x*, see Figure 1, gives a global view of the modulation effects. The modulations effects are shown by the evolution of lattice parameters at the transition: an optimization of the structure packing along *b* and a compensative dilatation of the inter-ribbon axis. The evolution of the incommensurate modulation versus $x > 0.7$ denotes the flexible interactions between modulated Bi/M/O-based ribbons and the surrounding tetrahedral groups as a function of the average size of the XO_4 groups.

Motif Ordering versus *x*. From the crystallographic point of view, the role of the modulation involves different sets of equivalent positions splitting, Figure 9. Let us only consider the framework based on double $[BiCu_2O_2]^{3+}$ ribbons. They are shown in Figure 9a projected along their infinite [0 1 0] axis for $BiCu_2PO_6$ and along the [0 0 1] axis in Figure 9b. There are $Z = 2$ "chain motifs = m" related by symmetry in the basic unit cell ($b \approx 5.2$ Å). Figure 9c shows the $x = 0.87$ case, assuming a commensurate $q = 1/4$ b* modulation with care of simplification ($Z = 8$). Starting from the initial motif (labeled m1 and located in the unit cell at $t = 0$), the super space group $Xbmm(0\gamma0)$ s00 generates at $t = 0$ and $t = 1/2$ equivalent motifs m0. In the same way, the motifs m2 at $t = 1/4$ and $t = {}^3/_4$ are equivalent, but distorted, compared to m1, by the modulation effects. In the 4×*b* supercell, m1 and m2 are arranged as shown in Figure 9c. The $q = 1/4$ b* approximation is rigorously false, and an incommensurate modulation gives rise to a set of four subsequent motifs at $t0$, $t0 + q$, $t0 + 2q$, $t0 + 3$q. Therefore, considering smooth, continuous, modulated functions for the Bi−Cu−O ribbon displacements, the unit cell at $t + 1/4$ should show structural features nearly similar to that at $t + q$. Of course, the main difference between commensurate and non-commensurate modulations is the modification of the set of four subsequent unit cells, all along the *b* axis.

As already discussed, for $x = 1$, $BiCu_2VO_6$ shows a commensurate supercell assorted with a symmetry lowering to monoclinic (space group $P2_1/n$).[12] Then according to this space group, the initial motif m is split in two submotifs m1 and m2 with $Z = 4$ and $Z = 2$ multiplicities, respectively, arranged as shown in Figure 9d. The global view of the ordering of variable motifs pictures well the inter- and intraribbon modulation change mainly driven by both the mean $(XO_4)^{3-}$ size and the flexibility of $[BiCu_2O_2]^{3+}$ ribbons. Their cooperative effects are driven by the structural change arising with the P for V substitution. Thus, it appears informative to have a careful look at the Chains/XO_4 interactions versus *x*.

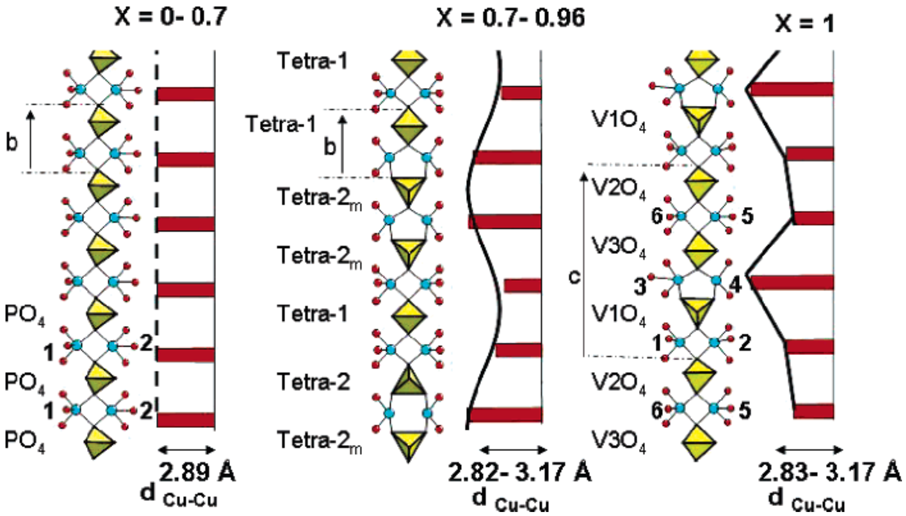

Figure 8. Orientation of the P/VO_4 groups between the Cu−Cu ladder rungs in the three subsequent domains along *x*. For the second domain, the most probable tetrahedra are reported by analogy with tetra-1, tetra-2, and tetra-2_m occupancies versus *t*. The bar graph shows the Cu−Cu separation along the *b* axis. Its smooth sinusoidal envelope pictures the modulated feature for $x = 0.87$, while the commensurate tripling for $x = 1$ is shown by straight lines and sharp angles.

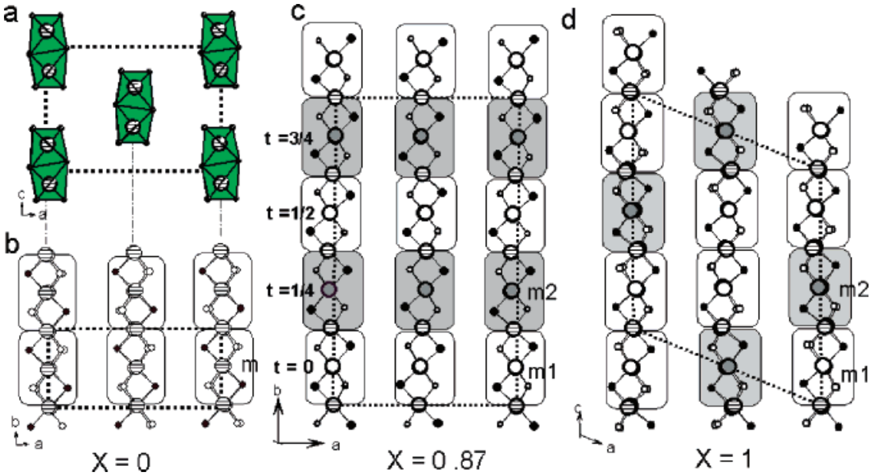

Figure 9. View of the $[BiCu_2O_2]^{3+}$ ribbons: (a) perpendicular to *b*; (b) perpendicular to *c* for $BiCu_2PO_6$ with evidence of the elementary motif m; (c) approximation to $q = 1/4$ b* for $x = 0.87$ with the arrangement of the two independent motifs m1 and m2 in the four-fold unit cell with respect to the *Xbmm*(0γ0) s00 super symmetry; (*d*) new arrangement of m1 and m2 in the triple monoclinic unit cell for $BiCu_2VO_6$ according to the space group $P2_1/n$.

Magnetic Properties

The geometrical existence of Cu^{2+} two-leg zigzag ladders (mentioned above) is an additional exciting characteristic of these series of compounds. From the magnetic point of view, the possible $S = {}^1/_2$ spin-ladder behavior would be of greatest interest in the field of new, low-dimensional quantum materials. Up to now, only $BiCu_2VO_6$ has been investigated by means of magnetic susceptibility, heat capacity, and neutron inelastic-scattering measurements.[13] A singlet ground state with a spin-gap has been confirmed, and the triple, narrow-band structure in the observed spectrum has been assigned as a probable result of the unit cell tripling involving three independent Cu−Cu pairs forming the rungs of the ladders.[12] At least the hypothesis of infinite $S = {}^1/_2$ magnetic chains running along the ladder legs is not acceptable, leading to a gapless continuum in the excitation spectrum. Therefore, the thermal activated susceptibility of $BiCu_2VO_6$ has been approximated by a Heisenberg $S = {}^1/_2$ antiferromagnetic dimer behavior, and the poor matching of experimental and theoretical plots did not take into account the strong interdimer couplings expected for ladders. This section is then dedicated to a brief examination of the thermal susceptibility of $BiCu_2(P_{1-x}V_x)O_6$ for *x* going through the modulated compositions ($x = 0$, 0.2, 0.8, and 1).

The thermal susceptibilities for the four investigated compositions are shown in Figure 10a. From the simple observation of the pronounced thermal activated character of $\chi_m(T)$, for $x = 0$, 0.2, and 1 a spin-gap behavior can be deduced. However, the $x = 0.8$ case is more questionable and will be discussed later. As already pointed out for $BiCu_2VO_6$, the single-dimer analysis using the Heisenberg $S = {}^1/_2$ Bleaney Bowers model,[28] derived from the Hamiltonian $H = -JS_aS_b$, does not match correctly for the four plots. To consider the probable contribution of interaction between dinuclear units, two treatments have been subsequently applied. First, we considered the intervention of weak interactions, zJ', similar to temperature-dependent θ_T Weiss corrections. For $S = {}^1/_2$ dimers we have:

$$\theta_T = \frac{zJ'}{k} \times 2[3 + \exp(-J/kT)]^{-1}$$

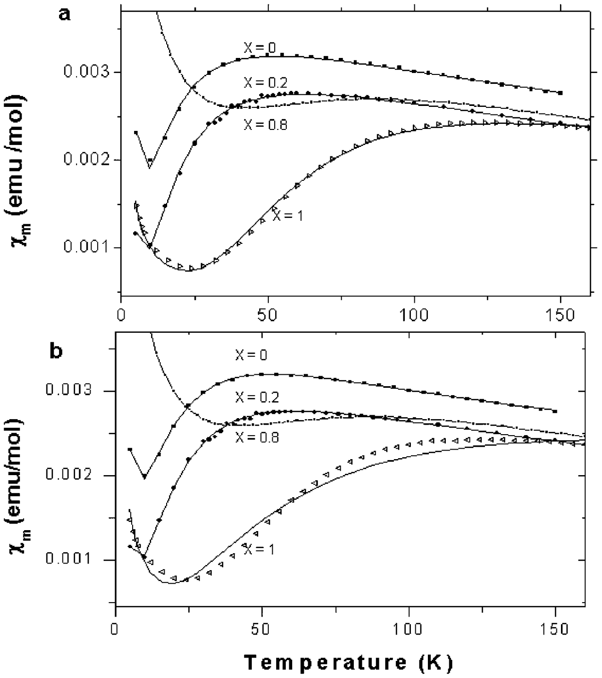

Figure 10. Molar susceptibility versus temperature for $x = 0$, 0.2, 0.8, and 1 fitted using: (a) the modified Bleaney Bowers model (continuous line) and (b) the $S = {}^1/_2$ two-leg ladder model (continuous line). The gapless $x = 0.8$ data (scattered line) did not fit any of the models.

and

$$\chi_m = \frac{2N\beta^2g^2}{kT(3 + \exp(-J/kT) - 2zJ'}(1 - \rho) + \frac{2(N\beta^2g^2)\rho}{3kT[S(S + 1)]} + N\alpha \quad (1)$$

where *k* is the Boltzmann constant, β is the Bohr magneton, ρ is the ratio of paramagnetic impurities, *J* is the intradimer exchange interaction and $N\alpha$ is the temperature-independent paramagnetism (TIP). In the second term which corresponds to the paramagnetic contribution, $S = {}^1/_2$ for Cu^{2+} cations This rigorous treatment did not converge for any of the three compounds. Only the addition of a temperature-independent Weiss-term corresponding to intramolecular interactions yields correct matching for $x = 0$, 0.2, and 1. The modified Bleaney−

---

(28) Bleaney, B.; Bowers, K. D. *Proc. R. Soc.* (*London*) **1952**, *Ser. A214*, 451.

Table 7. Results of the $\chi(T)$ Fits Using Two Models

	X = 0	X = 0.2	X = 1
g^a	2.27	2.12	2.03
	Bleaney Bowers + Weiss term (eq 1)		
J/k (K)	−38.3(1)	−35.8(3)	−142.5(2)
θ (K)	−244(2)	−222(2)	−118(2)
ρ (%)	6.8(1)	9.6(1)	8.3(4)
$N\alpha$	0.00026(1)	0.00080(1)	0.00047(1)
	Two-Leg Ladder (eq 2)		
A (emu·K$^{-1/2}$)	0.0170(2)	0.0152(1)	0.024(6)
Δ/k (K)	32.9(1)	30.2(1)	92(3)
ρ (%)	0.51(2)	0.94(2)	0.085(8)
$N\alpha$	0.00008(1)	0.00035(1)	0.00014(4)

[a] The g values have been determined by ESR spectroscopy.

Bowers equation is then given by:

$$\chi_m = \frac{2N\beta^2 g^2}{k(T-\theta)(3+\exp(-J/kT))}(1-\rho) + \frac{2(N\beta^2 g^2)\rho}{3kT[S(S+1)]} + N\alpha \quad (2)$$

The results of the fits are given in Table 7. One should somewhat notice that the refined θ values are greater than the corresponding J/k values involving strong interdimer couplings under the restriction of a meaningful model. While the used model is only appropriate for weak intermolecular couplings, the good agreement of the fits at least implies the strong importance of the neighboring species related to a simple dimer analysis. Thus, it strongly suggests the possibility of true spin-ladders. Also notice the stronger J/k value for $x = 1$, which denotes a drastic change in the tripled cell where three kinds of independent dimers coexist.

The first $\chi(T)$ measurements on $SrCu_2O_3$ by Azuma et al.[29] were modeled by the low-temperature approximation of a $S = {}^1/_2$ two-leg spin-ladder derived by Troyer, Tsunetsgu, and Würtz[30] used in our work as follows:

$$\chi_m = AT^{-1/2}\exp(-\Delta/kT)(1-\rho) + \frac{2(N\beta^2 g^2)\rho}{3\,kT[S(S+1)]} + N\alpha \quad (3)$$

Once more, the first term describes the spin-ladder susceptibility while a paramagnetic contribution and TIP are considered in the second and third terms, respectively. In the spin-ladder contribution, A is a preexponential term and Δ/k is a finite spin-gap. The results of the fits for $x = 0$, 0.2, and 1 are shown in Figure 10b and are listed in Table 7. The good matching of eq 2 for $x = 0$ and 0.2 is reinforced by the realistic values refined for the ρ paramagnetic ratio and $N\alpha$ TIP. The refined gap values are 32.9 and 30.2 K, very comparable despite the lattice parameters differences. It is obvious that the gap values depend on the structural and chemical features of the concerned solids, e.g. $\Delta/k = 600$ K for CaV_2O_5 and 17 K for MgV_2O_5, both V^{4+} ladder systems with similar crystal structures.[31] If one assumes spatially isotropic exchange interactions $J_\perp = J_\parallel$ within isolated two-leg ladders, then using $\Delta/J \approx 0.5$ appropriate to this case[30] yields $J/k = 65.8$ and 60.4 K, respectively.

This model is inappropriate for $BiCu_2VO_6$, Figure 10b, but in that case one should remember that a triple, narrow-band spectrum has been observed due to the symmetry lowering from orthorhombic to monoclinic associated with a unit cell tripling. The susceptibility for the $x = 0.8$ compound shows no evidence of a finite gap but rather resembles the chain magnetism. From the structural point of view, the modulated regime of this compound leads to a continuous distribution of Cu−Cu separations along the ladders, i.e., 3.15 to 3.32 Å along the legs and 2.82 to 3.17 Å along the rungs for $x = 0.87$. Intuitively, the resulting fundamental state should lead to overlapping of broadened band which could yield to a gapless continuum in the excitation spectrum. Then these series of compounds would exhibit a continuous evolution from ladder systems to gapless systems driven by broadening of bands of structural origin. This evolution is driven by the phosphate for greater vanadate substitution which strongly influences the neighboring copper zigzag ladder as well as Bi−M−O double ribbons structure.

Acknowledgment. We sincerely thank Dr. Emmanuelle Suard (ILL, Grenoble, France) and Dr. Hervé Vezin (LCOM, UMR CNRS 8009, UST Lille, France) for neutron diffraction experiments and EPR measurements, respectively. We also thank Dr. Pascal Roussel (LCPS, UMR CNRS 8012, France) for helpful discussion. Vaclav Petricek could participation on this work thanks to the support from the Grant Agency of the Czech Republic, Grant 202/03/0430.

Supporting Information Available: The CIF file corresponding to the 4D refinement for $x = 0.87$ and the 3D treatment for $x = 0.32$ (XRD single crystal) and 0.6 (ND powder data); additional graphs and tables related to our work. This material is available free of charge via the Internet at http://pubs.acs.org.

JA0631091

---

(29) Azuma, M.; Hiroi, Z.; Takano, M.; Ishida, K.; Kitaoka, K. *Phys. Rev. Lett.* **1994**, *73*, 3463.

(30) Troyer, M.; Tsunetsugu, H.; Würtz, D. *Phys. Rev. B*5 **1994**, *50*, 1351.

(31) Ueda, Y. *Chem. Mater.* **1998**, *10*, 2653.